Asociación Argentina
de Mecánica Computacional

Mecánica Computacional Vol XXX, págs. 193-208 (artículo completo)
Oscar Möller, Javier W. Signorelli, Mario A. Storti (Eds.)
Rosario, Argentina, 1-4 Noviembre 2011

A NEW CAVITATION MODEL FOR THE SIMULATION OF PISTON-RING LUBRICATION

Roberto F. Ausas[a], **Mohammed Jai**[b], **Ionel S. Ciuperca**[c] **and Gustavo C. Buscaglia**[a]

[a]*Instituto de Ciências Matemáticas e Computação, Universidade de São Paulo, Av. do Trabalhador Sãocarlense 400, 13560-970 São Carlos, SP, Brazil, rfausas@gmail.com*

[b]*CNRS-UMR 5208, Mathématiques, INSA de LYON, Bat Leonard de Vinci, F-69621 Villeurbanne, France, mohammed.jai@insa-lyon.fr*

[c]*CNRS-UMR 5208, Université Lyon 1, MAPLY, Bat. 101, 69622 Villeurbanne cedex, France, ciuperca@maply.univ-lyon1.fr*

Keywords: Hydrodynamic lubrication, Cavitation, Elrod–Adams model, Piston–rings.

Abstract. The only strictly conservative cavitation model in hydrodynamic lubrication, is the Elrod–Adams model. In this model, the so called JFO conditions (due to Jacobson & Floberg and Olsson) are imposed at the cavitation boundary which is an unknown of the problem. Unfortunately, this lubrication model is not well–suited for the simulation of cavitated regions in which the fluid film is attached to just one of the participating surfaces, as happens in piston–ring assemblies. In these regions, the Elrod-Adams model yields a lubricant transport velocity that is half of the physically-realistic value. This has been known for about three decades, but attempts at correcting the numerical models so as to increase the transport velocity have up to now failed. In this communication we first show the reasons for these attempts to have failed, which come from a loss of uniqueness of the associated exact mathematical problem. Then, we introduce a variant of the Elrod–Adams model that has a unique solution while still allowing for the transport velocity in the cavitated region to be adjusted at physically realistic values. Finally, a first numerical implementation of this new model is discussed, together with test–case results.

1 INTRODUCTION

Piston–rings/liner contacts amount for a large part of the total power loss due to friction among the many reciprocating components present in internal combustion engines. Their main function is to seal the space between the piston and the liner acting as slider bearings subjected to alternating motion. These systems have been thoroughly studied before (see for instance Priest (1996), Priest and Dowson (1999) and Priest (2000)).

The key issue in the simulation of such lubricated devices is the treatment of cavitation phenomena by means of incorporating appropiate mass–conservative conditions at the *unknown* cavitation boundaries. Cavitation may occur for several reasons: as a result of a divergent film geometry, due to a positive squeeze (i.e., a transient variation of the gap between the lubricated surfaces) and also at microtextures.

Two models are predominantly used in hydrodynamic lubrication: the Reynolds model and the Elrod–Adams model Elrod and Adams (1974). The former, easier to implement numerically, though being non conservative, gives reasonable predictions in some cases and is thus still used in practice. However, as shown in Ausas et al. (2007), for problems including transient effects and/or microtextures, this model is certainly not recommended. In those cases, the importance of using a conservative model such as the Elrod–Adams model have been shown by means of several numerical examples in Ausas et al. (2007, 2009). In this model, the conditions proposed by Jakobson and Floberg (1957) and Olsson (1965) are applied at the cavitation boundary to enforce mass conservation. However, due to the highly non–linear nature of the problem, numerical implementations of this model are more proclive to numerical instabilities and for this reason is not always used.

Piston–ring/liner systems need special consideration. In these systems, a thin lubricant film remains essentially attached to the liner, being this a fundamental difference with respect to other reciprocating components, like journal or thrust bearings in which the amount of available oil in the non–pressurized region, which is insufficient to fill the entire separation between the lubricated surfaces, cannot be assigned to just one of them. Mathematically, the Elrod–Adams model yields a lubricant transport velocity in the cavitated region that is half of the physically-realistic value. This has been known for several decades, but not seriously addressed until the work of Buscaglia et al. (2011) in which a new model is proposed whose numerical implementation is presented here.

By way of outline, after this intoduction, the mathematical model and the governing equations for the new model are presented. Next, the numerical procedure, for the one dimensional case is presented. We restrict ourselves to the case of a constant sliding velocity for the sake of simplicity. In the results section, several problems are presented: First, a simple case for which an exact solution can be computed, consisting in a single ring with a smooth liner, is solved to show convergence of the numerical predictions as a function of the mesh size. Second, the case of a moving texture on the liner is considered. In this case, two rings are simulated. Finally, some conclusions are drawn.

2 MATHEMATICAL MODEL

2.1 The new model - One dimensional case

We restrict ourselves to the one dimensional case which is more amenable for numerical implementation as shown in the next section. The numerical formulation in the two dimensional case is still the subject of ongoing work. We also consider the case of velocity $S > 0$. The case of negative velocity can be obtained straightforwardly. In the one dimensional case the cavitation boundary is represented by a set of points in the computational domain $\Omega = [x_\ell, x_r]$. For the sake of simplicity in the exposition we consider just one ring and thus a unique central pressurized region with boundary points denoted by $x = \alpha(t)$ and $x = \beta(t)$ (see figure 1). The extension to consider multiple rings, each one with a pressurized region and corresponding boundaries can be obtained without major difficulties. In fact, in the results section we present numerical examples with two rings.

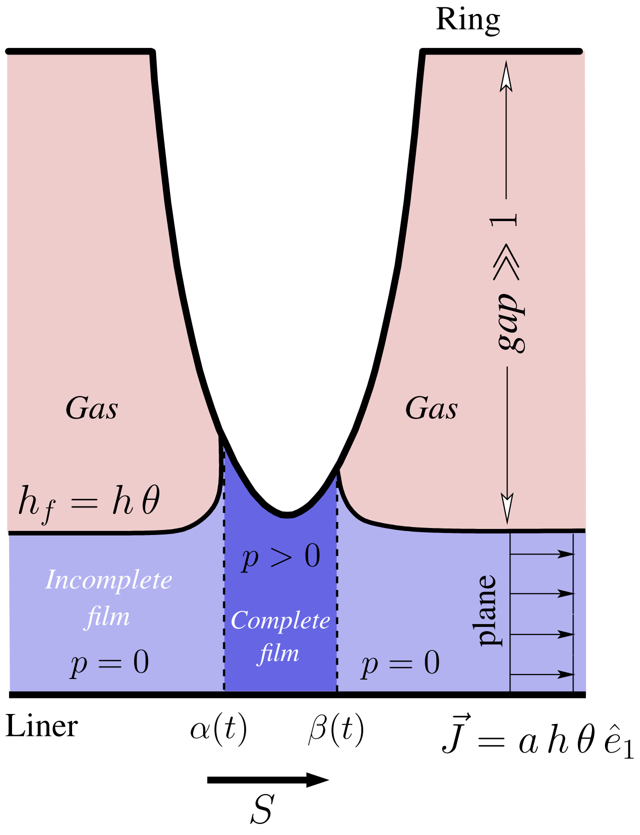

Figure 1: Problem setting for the piston–ring/liner system.

We consider an initial condition given by $\alpha_0 = \alpha(t = 0)$ and $\beta_0 = \beta(t = 0)$, the left and right boundaries of the pressurized region, together with the saturation field $\theta_0(x) = \theta(x, t = 0)$ given for $x < \alpha_0$ and $x > \beta_0$ (see figure 1). It is assumed that the solution of the Reynolds equation

$$\partial_x \left(h^3 \partial_x p\right) = \left(\frac{S}{2}\, \partial_x h \,+\, \partial_t h\right) \qquad \text{with} \qquad p(\alpha_0, t = 0) = p(\beta_0, t = 0) = 0 \tag{1}$$

yields a non–negative pressure p in (α_0, β_0). The equations for the velocities of the boundary fronts $\alpha'(t)$ and $\beta'(t)$ result from mass conservation at these points, yielding,

$$\alpha'(t) = \frac{-h^3(\alpha)\partial_x p(\alpha^+, t) + \frac{S}{2} h(\alpha)\left[1 - 2a\theta(\alpha^-, t)\right]}{h(\alpha)\left[1 - \theta(\alpha^-, t)\right]} \tag{2}$$

$$\beta'(t) = \frac{-h^3(\beta)\partial_x p(\beta^-, t) + \frac{S}{2} h(\beta)\left[1 - 2a\theta(\beta^+, t)\right]}{h(\beta)\left[1 - \theta(\beta^+, t)\right]} \tag{3}$$

Finally, the equation for $\theta(x,t)$ in the cavitated region reads

$$\partial_t(\theta\, h) + a\, S\, \partial_x(\theta\, h) = 0 \tag{4}$$

for which boundary conditions are needed at the left boundary $\theta(x_\ell, t) = \theta_{\text{in}}(t)$ and at $\beta(t)$ whenever $\beta'(t) < S$ (which is in general the case).

The Elrod–Adams model and the new model being studied here differ in the treatment of the rupture boundary, at which some of the fluid detaches from the wall because otherwise the pressure would become negative. Since, further away from the rupture boundary, the fluid remains attached to the lower wall and travels at velocity S, we have to take $a = 1$ in (4). In the Elrod–Adams model, a physically uncorrect value of $a = 1/2$ is taken.

As previously mentioned, the new model aims at establishing a well–posed mathematical model that consider a physically correct transport velocity $a\, S$ with $a \neq 1/2$. In particular, we consider here the case $a = 1$, but, the general case with $a \in [1/2, 1]$ is discussed in Buscaglia et al. (2011). For the new model to be well–posed, an additional condition at the rupture boundaries is needded as we shall see.

Since, $\partial_x p(\beta^-(t), t) \leq 0$ (because $p \geq 0$ on $\Omega_+(t)$), we obtain from equation (3) that

$$\theta(\beta^+(t), t) \geq F(\beta'(t)) = \begin{cases} \frac{\frac{S}{2} - \beta'(t)}{a\, S - \beta'(t)} & \text{if } \beta'(t) \leq 0 \\ \frac{1}{2\, a} & \text{if } \beta'(t) > 0 \end{cases} \tag{5}$$

This condition implies that $\theta(\beta^+(t), t)$ must satisfy

$$\max\{0, F(\beta'(t))\} \leq \theta(\beta^+(t), t) \leq 1 \tag{6}$$

If $a = 1/2$, this conditions reduces to $\theta(\beta^+(t), t) = 1$. If $a > 1/2$ then $\theta(\beta^+(t), t)$ is not fully determined from condition (6). For any given $\beta'(t)$ there is a finite interval of values that satifies (6) and each of these values leads to a different solution of the problem. *This explains the lack of uniqueness of the model so far when $a \neq 1/2$ and the need for an additional condition in order to have a unique solution.*

To recover the uniqueness, among the multiple values possible for $\theta(\beta^+(t), t)$ we propose a specific choice that leads to a well–posed problem. This specific choice for our case, with $a = 1$, is to take $\theta(\beta^+(t), t)$ equal to $F(\beta'(t))$.
Before passing to the numerical assessment of the model, it can be noticed that by using equation (3) with this choice for θ at $x = \beta$, the corresponding to $\beta'(t) \leq 0$ leads to a zero pressure gradient and no equation for the velocity $\beta'(t)$. This introduces difficulties in the numerical implementation of such model that are explained in the next section.

3 NUMERICAL METHOD

The numerical procedure is an explicit algorithm very much based on that presented by Buscaglia et al. (2010) previously, though generalized to deal with more complex boundary conditions and shapes.

We consider a time step Δt. The computational domain $[x_\ell, x_r]$ is divided into cells of uniform size Δx. The time step of a discretized variable is shown as a superscript and the nodal value as a subindex. Let consider, α^n and β^n the discrete values of $\alpha(t^n)$ and $\beta(t^n)$ respectively, not coincident with the mesh nodes at positions X_i. At time level n, the computational domain is divided into the set of cavitated–node indices C^n ($X_i < \alpha^n$ or $X_i > \beta^n$) and the set of pressurized–node indices P^n ($\alpha^n < X_i < \beta^n$). For given $\{\theta_i^n\}_{i \in C^n}$, the numerical procedure to find the new pressure and saturation field and the new position of the cavitation boundaries is explained in what follows. In figure 2 we illustrate the finite volume discretization used for a particular case with $\alpha' < 0$ and $\beta' < 0$.

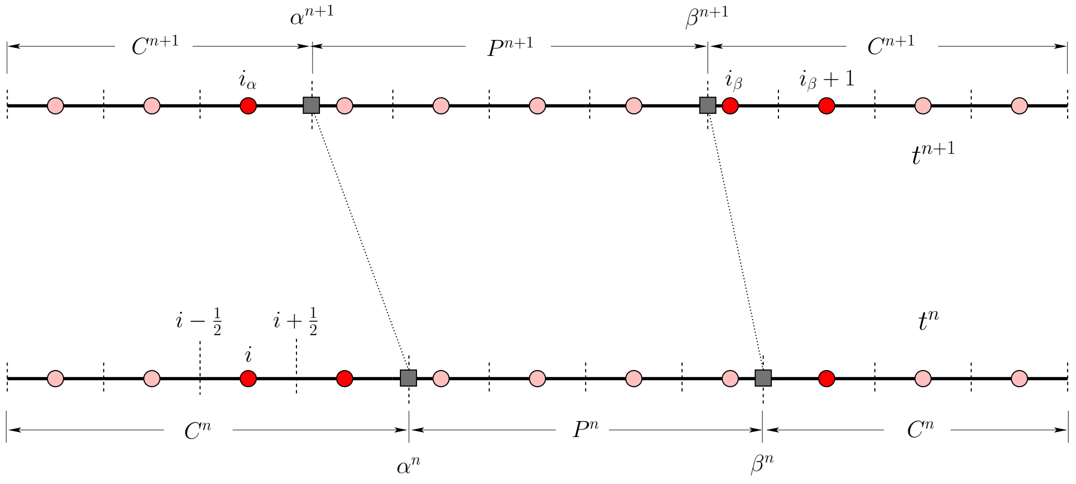

Figure 2: Scheme of the finite volume discretization for the one dimensional computational domain.

1. **Numerically solve Reynolds equation for p^n:** A finite volume solver for $\{p_i^n\}_{i \in P^n}$ is used to solve equation (1), where P^n is the set of pressurized–node indices. The conditions $p^n(\alpha^n) = p^n(\beta^n) = 0$ are imposed placing two virtual nodes at the positions α^n and β^n.

2. **Compute α^{n+1} and β^{n+1}:** Here we use explicit updating

$$\alpha^{n+1} = \alpha^n + \Delta t\, \alpha', \qquad \beta^{n+1} = \beta^n + \Delta t\, \beta' \tag{7}$$

   where α' and β' are obtained from (2) and (3), considering $\theta(\beta^+, t) = 1/2$, i.e.,

$$\beta' = -2\, h^2(\beta^n)\, \partial_x p^n(\beta^{n-}) \tag{8}$$

   This is correct if the resulting β' is positive (and $< S$, which is always the case in the considered examples). If $\beta' < 0$, this implies that $\partial_x p^n(\beta^{n-}) > 0$ and thus that p^n is negative to the left of β^n. In this case β^{n+1} is chosen such that $\beta^{n+1} \neq \beta^n$ for which, we find β^{n+1}, such that $p^n(\beta^{n+1}) = 0$ considering a linear interpolation of the nodal values of p^n. We expect first-order convergence with Δt, which is indeed suggested in the numerical tests performed.

3. **Numerically solve the transport equation for θ^{n+1}:** A finite volume solver is used. Notice that (4) is an evolution equation (in time) on a domain that is time–dependent. The finite volumes thus move according to α' and β' and the result is projected (conserving mass) onto the fixed nodal positions. Clearly, the finite volumes immediately next to the cavitation boundaries (in red in figure 2) have to be dealt differently from the rest of the (standard) finite volumes (in pink). This is now explained for the particular situation illustrated in figure 2 corresponding to $\alpha' < 0$ and $\beta' < 0$ and where the cavitation boundaries cross the cell faces from one step to the other.

- For the standard finite volumes, we use a first–order (donor cell) scheme as follows

$$h_i^{n+1}\,\theta_i^{n+1}\,\Delta x = h_i^n\,\theta_i^n\,\Delta x + S\,\left(h^n_{i-\frac{1}{2}}\,\theta^n_{i-1} - h^n_{i+\frac{1}{2}}\,\theta^n_i\right)\Delta t \tag{9}$$

  where $h^n_{i\pm\frac{1}{2}}$ is the value of h^n evaluated at position $X_{i\pm\frac{1}{2}}$.

- For the finite volumes next to the cavitation boundaries we have:
  Denoting by $i_\alpha \in C^{n+1}$ the first finite volume to the left of α^{n+1}, the value of $\theta^{n+1}_{i_\alpha}$ is computed from

$$\begin{aligned} h^{n+1}_{i_\alpha}\,\theta^{n+1}_{i_\alpha}(\alpha^{n+1} - X_{i_\alpha-\frac{1}{2}}) &= h^n_{i_\alpha}\,\theta^n_{i_\alpha}(\alpha^n - X_{i_\alpha-\frac{1}{2}}) + h^n_{i_\alpha+1}\,\theta^n_{i_\alpha+1}(\alpha^n - \alpha^{n+1}) + \\ &+ \left[S\,h^n_{i_\alpha-\frac{1}{2}}\,\theta^n_{i_\alpha-1} - (S-\alpha')\,h(\alpha^n)\,\theta^n_{i_\alpha}\right]\Delta t \end{aligned} \tag{10}$$

  Denoting by $i_\beta \in C^{n+1}$ the first finite volume to the right of β^{n+1}, the values of $\theta^{n+1}_{i_\beta}$ and $\theta^{n+1}_{i_\beta+1}$ are computed from

$$\theta^{n+1}_{i_\beta} = \theta(\beta^+, t^{n+1}) = \frac{\frac{S}{2} - \beta'(t)}{S - \beta'(t)} \tag{11}$$

$$\begin{aligned} h^{n+1}_{i_\beta+1}\,\theta^{n+1}_{i_\beta+1}\,\Delta x + h^{n+1}_{i_\beta}\,\theta^{n+1}_{i_\beta}(X_{i_\beta+\frac{1}{2}} - \beta^{n+1}) &= h^n_{i_\beta+1}\,\theta^n_{i_\beta+1}(X_{i_\beta+\frac{3}{2}} - \beta^n) + \\ &+ \left[(S-\beta')\,h^n_{i_\beta+\frac{1}{2}}\,\theta^n_{i_\beta+1} - S\,h^n_{i_\beta+\frac{3}{2}}\,\theta^n_{i_\beta+1}\right]\Delta t \end{aligned} \tag{12}$$

We proceed in a similar way for other cases that may arise when the cavitation boundaries do not cross the cell faces and the velocities $\alpha' > 0$ and $\beta' > 0$.

4 NUMERICAL RESULTS

4.1 Convergence test

We simulate a single ring with a parabolic shape moving with constant velocity $S = 1$ and a smooth liner. The computational domain is the interval $[0, 1]$. The distance between the two lubricated surfaces is given by

$$h(x) = 1 + (2\,x - 1)^2 \tag{13}$$

We consider two different situations corresponding to the following initial conditions

- $(h\,\theta)(x_\ell, t) = 0.65$, $\alpha_0 = 0.30$, $\beta_0 = 0.59$
- $(h\,\theta)(x_\ell, t) = 0.45$, $\alpha_0 = 0.25$, $\beta_0 = 0.55$

In these simple cases, the exact solution can be computed and then compared to the numerical predictions. First, in figure 3 we show the film profile at different times using a grid resolution $\Delta x = 0.0025$. For the first case, corresponding to $(h\,\theta)(x_\ell, t) = 0.65$, we show in figure 4 the position of the left and right fronts as a function of time using different grid resolutions, namely, $\Delta x = 0.01,\ 0.005,\ 0.0025,\ 0.00125$. A time step Δt equal to 0.001 is used for the first mesh. The Courant number is kept constant for the rest of the simulations for which the time step is

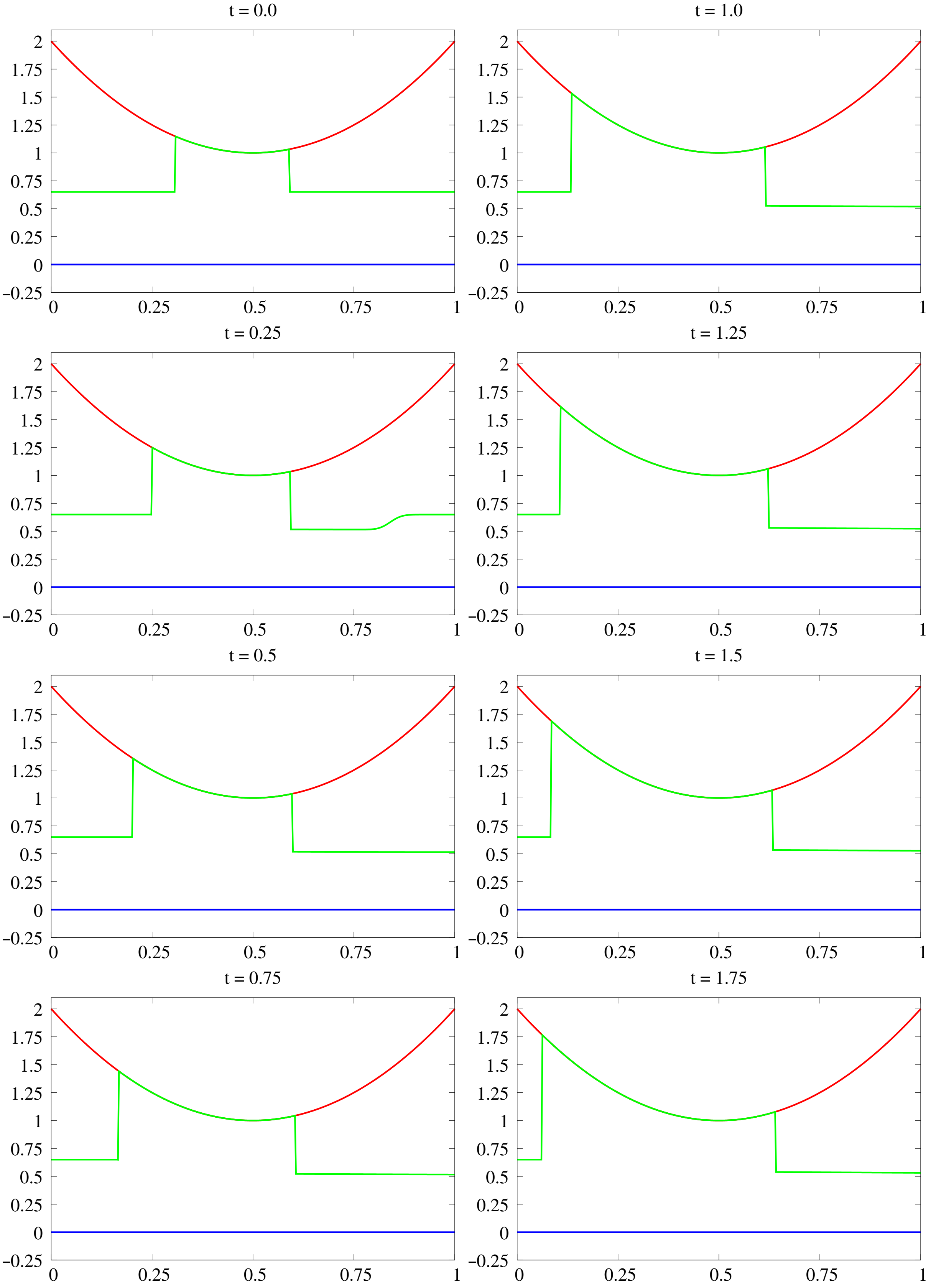

Figure 3: Film profiles at different times for the single ring test for $(h\,\theta)(x_\ell, t) = 0.65$.

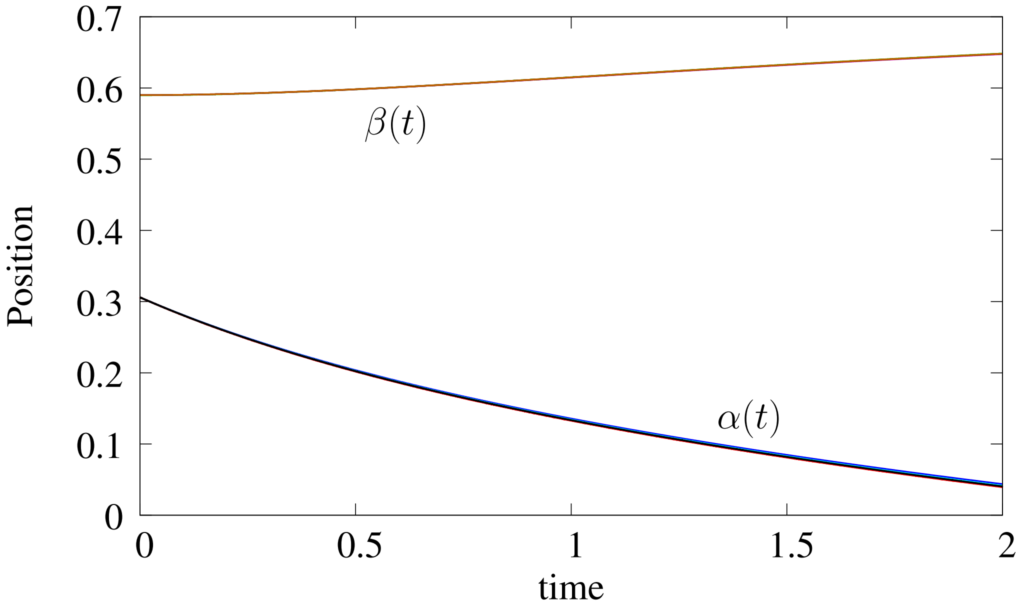

Figure 4: $\alpha(t)$ and $\beta(t)$ for different grid resolutions for the first case with $(h\,\theta)(x_\ell, t) = 0.65$.

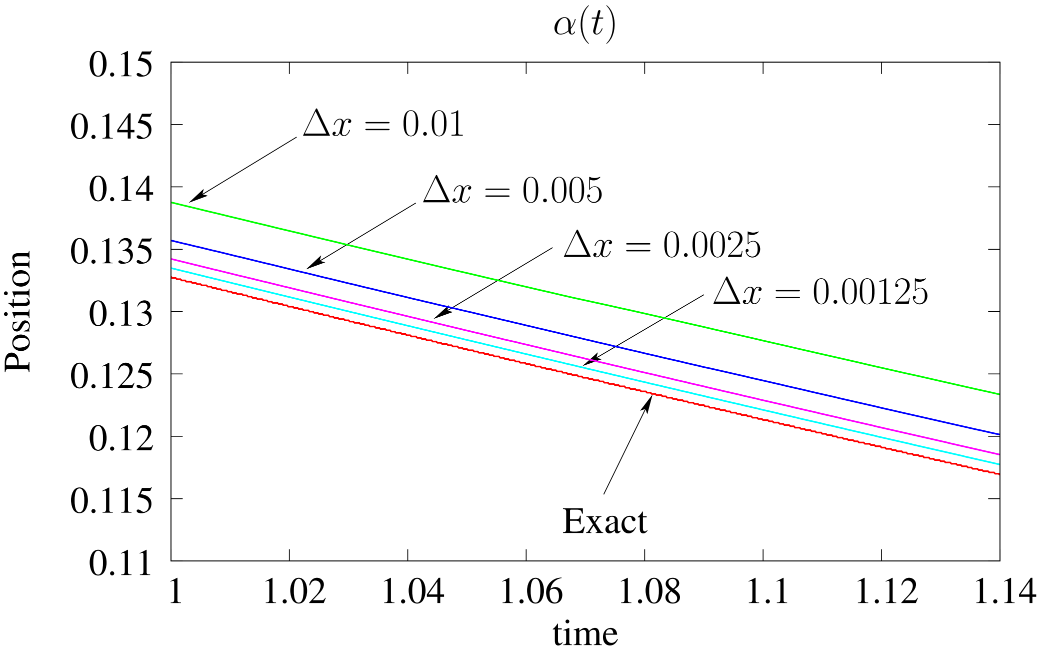

Figure 5: Detail $\alpha(t)$ for different grid resolutions for the first case with $(h\,\theta)(x_\ell, t) = 0.65$.

adjusted accordingly. A detail of figure 4 is shown in figure 5 to appreciate how the numerical solution converges to the exact one for the left (reformation) front. The convergence is similar for the right (rupture) front.

For the second case, corresponding to $(h\,\theta)(x_\ell, t) = 0.45$, in figure 6 we show the film profile at different times and in figure 7 we show the position of the left and right fronts as a function of time for the same grid resolutions used in the previous case. The reformation front moves to the right and the rupture front, initially moves to the right and at time t approximately equal to 1 it starts to move to the left. In this case, the pressurized region tends to shrink until it disappears. The differences between the exact and numerical solutions are better seen in the detail shown in figure 8 for the reformation front $\alpha(t)$ and in figure 9 for the rupture front $\beta(t)$ using the algorithm mentioned in section 3. Notice the stair–case like behavior of the solution. This behavior is due to the type of algorithm choosen to deal with the case of a negative velocity at a rupture boundary.

4.2 Textured–liner test

The aim in this case is to illustrate the differences between the new lubrication model and the Elrod–Adams model. The initial condition and geometry considered in this case is shown in figure 10. The computational domain is the interval $[-0.5, 1]$. The total distance between the two lubricated surfaces $h(x,t)$ has thus two contributions: one is the shape of the ring assembly $h_r(x)$ given by

$$h_r(x) = \begin{cases} 1 + 20\,(x - \frac{1}{4})^2 & \text{if } 0.025 < x < 0.475 \\ 1 + 20\,(x - \frac{3}{4})^2 & \text{if } 0.525 < x < 0.975 \\ 2 & \text{elsewhere} \end{cases} \tag{14}$$

and the other is the contribution of the moving texture on the liner, which is taken to be

$$h_t(x,t) = \max\{0,\ h_0 \sin[6(x-t)]\} \tag{15}$$

where h_0 is taken equal to 0.1. There are thus four fronts to be tracked in time whose initial positions are taken as

$$\alpha_0^{(1)} = 0.125, \quad \beta_0^{(1)} = 0.275 \tag{16}$$

$$\alpha_0^{(2)} = 0.625, \quad \beta_0^{(2)} = 0.775 \tag{17}$$

The mesh size Δx is set to 0.0015 and the time step Δt to 0.0001. The inlet film $h_f(x_\ell, t)$ is set to a fixed value of 0.67. To satisfy this boundary condition we adjust at each time step the value of $\theta(x = x_\ell, t)$ since $h(x = x_\ell, t)$ is not constant due to the moving texture. In figure 11 we show the film profile at different times.

We also simulate the same problem with the Elrod–Adams p–θ model. As mentioned before, this problem is important because the behavior of the second ring can be very much affected by the first (upstream) ring. In this case, in order to make a fair comparison, we consider an inlet film height $h_f(x_\ell, t)$ equal to 2×0.67, that corresponds in this model to the same inlet flow used for the simulations using the new model. Results are shown in figure 12. The are notorious differences between the two models that can be observed. First, since according to the Elrod–Adams model the texture travels at velocity $S = 1$ while the saturation field θ is transported with velocity $S/2$ in the cavitated region, the film profile results perturbed in the left region $(-0.5, \alpha^{(1)}(t))$, while for the new model the film profile remains flat. Second, the fronts moves with different velocities in each model, leading to a different temporal evolution of the pressurized region for each ring. We illustrate this difference in figure 13 where the pressure profiles for both models at selected times are plotted. Third, the new model predicts a discontinuity at the rupture boundaries $\beta^{(1)}$ and $\beta^{(2)}$ which does not occur with the Elrod–Adams model.

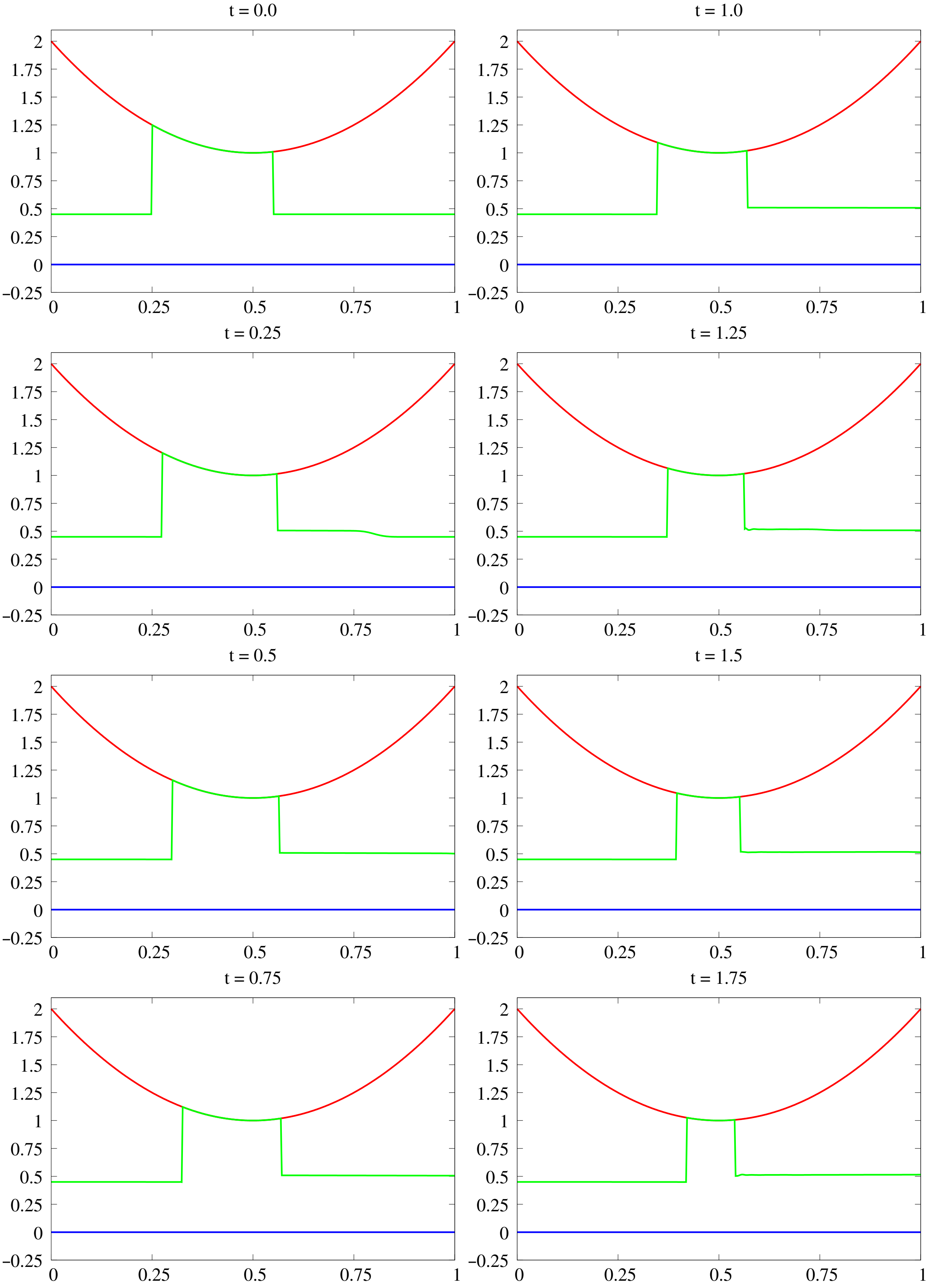

Figure 6: Film profiles at different times for the single ring test with $(h\,\theta)(x_\ell, t) = 0.45$.

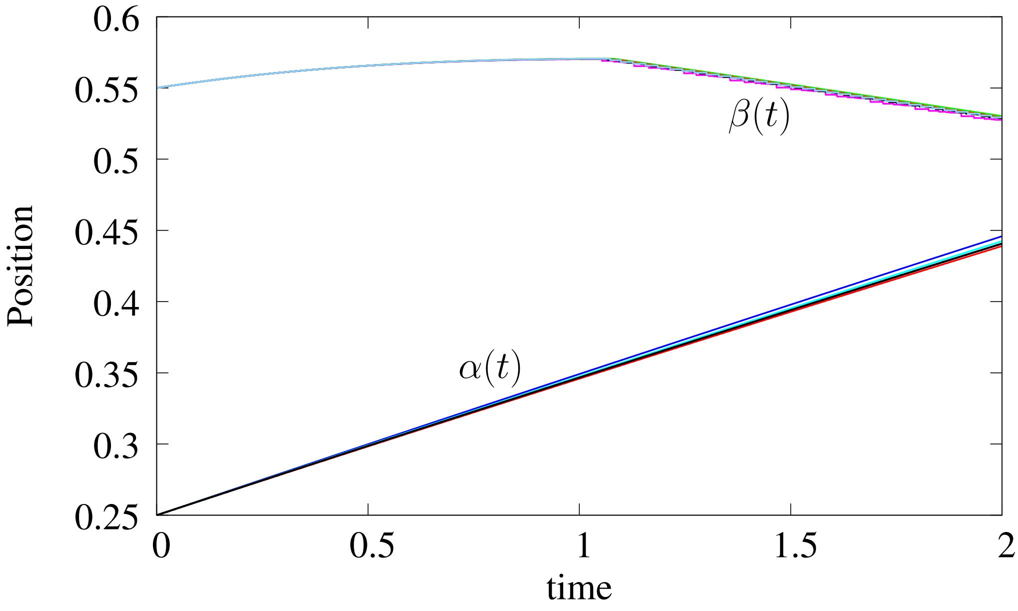

Figure 7: $\alpha(t)$ and $\beta(t)$ for different grid resolutions for the second case with $(h\,\theta)(x_\ell, t) = 0.45$.

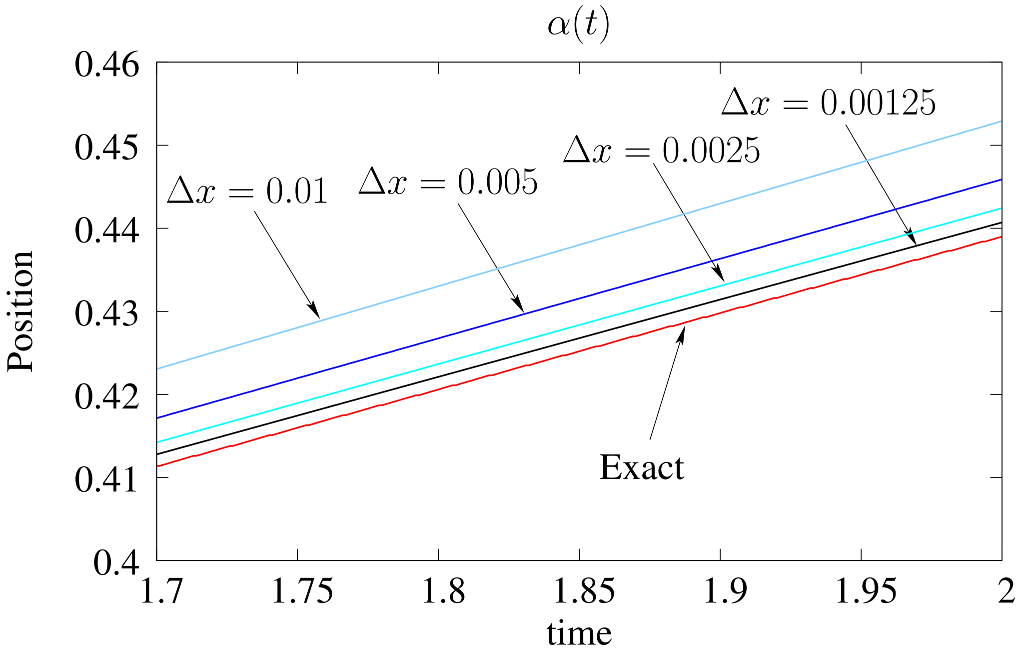

Figure 8: Detail of $\alpha(t)$ for different grid resolutions for the second case with $(h\,\theta)(x_\ell, t) = 0.45$

5 CONCLUSIONS

The main objective of this article has been the presentation of a numerical implementation of the new lubrication model recently introduced in Buscaglia et al. (2011) which can be seen as a variant of the Elrod–Adams model but deals in a more realistic way with the particularities of piston–ring/liner systems. The proposed algorithm for this new model is based on a finite volume scheme with an explicit tracking of the cavitation fronts so as to impose the appropiate boundary condition for the saturation field depending on the velocities of such fronts. Although

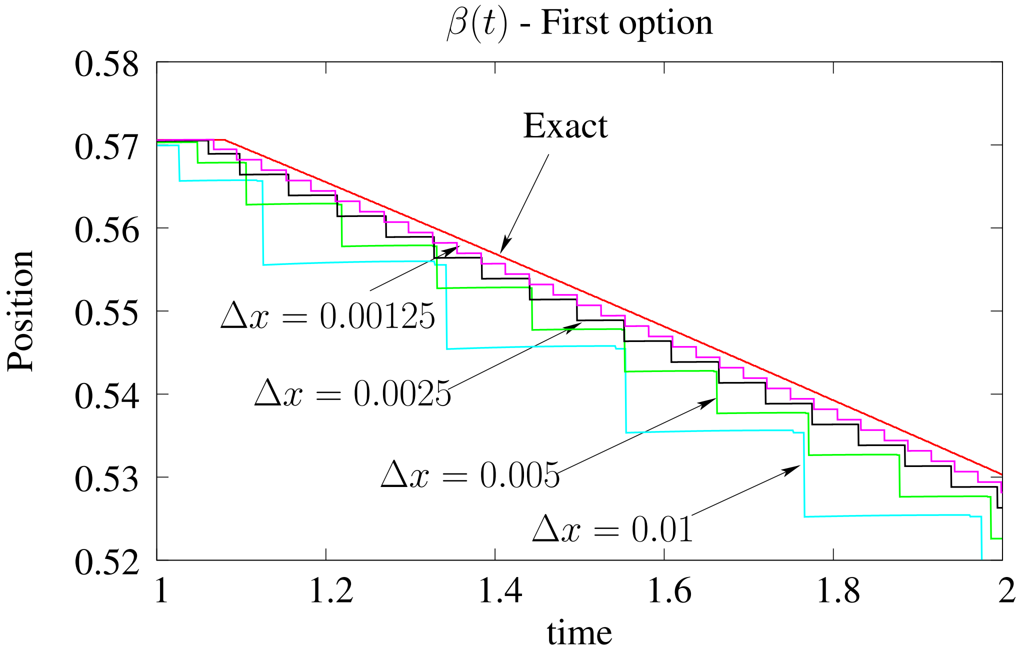

Figure 9: Detail of $\beta(t)$ for different grid resolutions for the second case with $(h\,\theta)(x_\ell, t) = 0.45$.

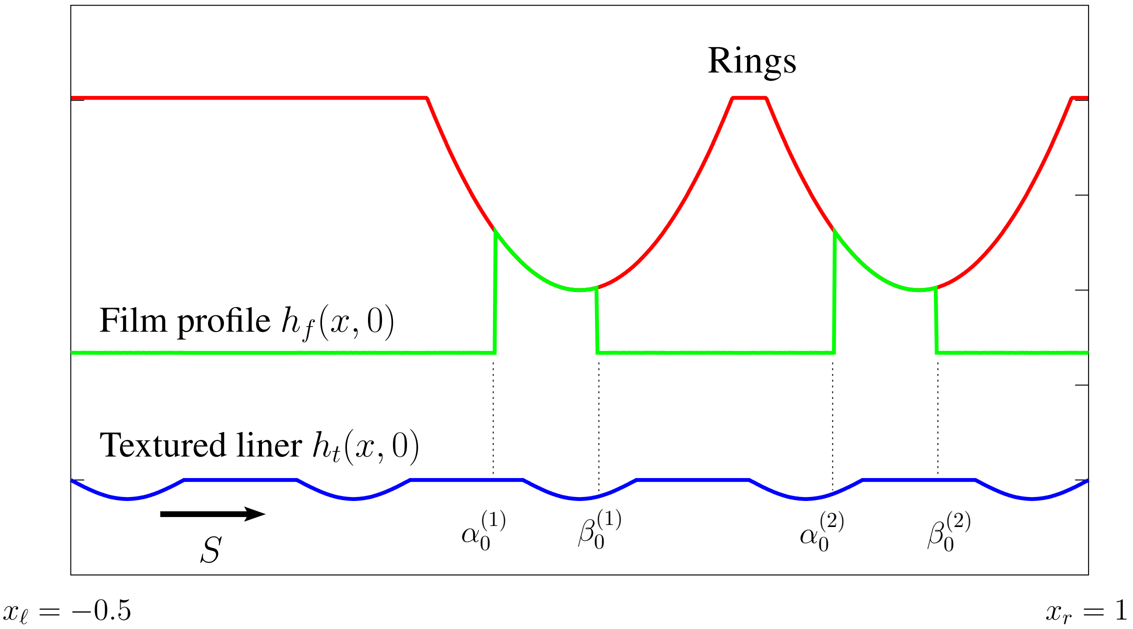

Figure 10: Initial condition for the textured liner test showing the two rings and the moving texture.

in this article we have focused on the one dimensional case with constant sliding velocity, the necessity for a new model is already observed. Three different tests have been presented. The first one, consisting in the simulation of a single ring of parabolic shape with a smoth liner, a problem for which an exact solution can be found, aimed to show that the proposed numerical procedure gives convergent solutions. The second test, that dealed with a more complicated setting, included two rings of parabolic shape and a moving texture of sinusoidal shape. In this case, a comparison to the Elrod–Adams model has been done to show the fundamental

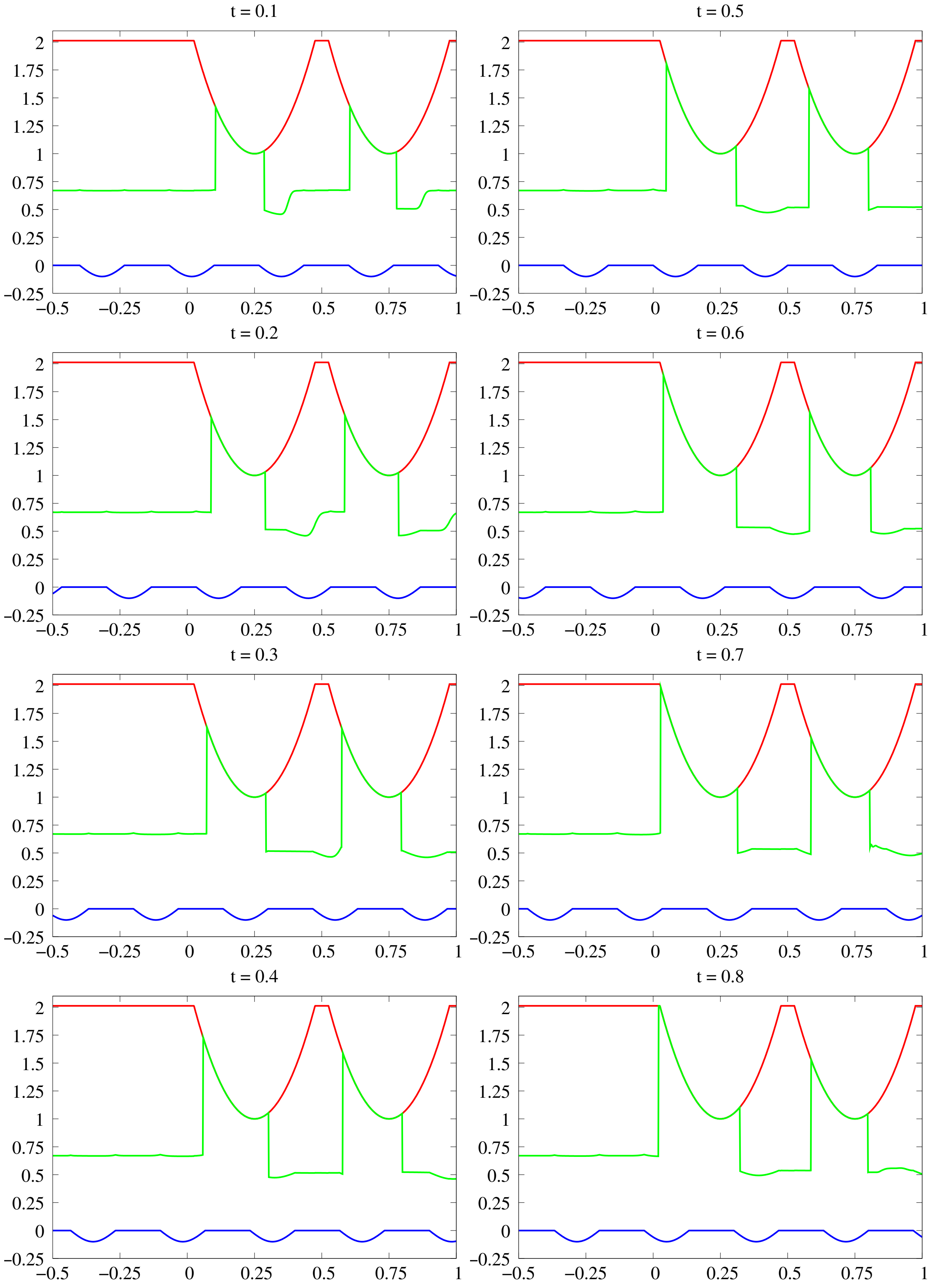

Figure 11: Film profiles at different times for the textured–liner test using the new model.

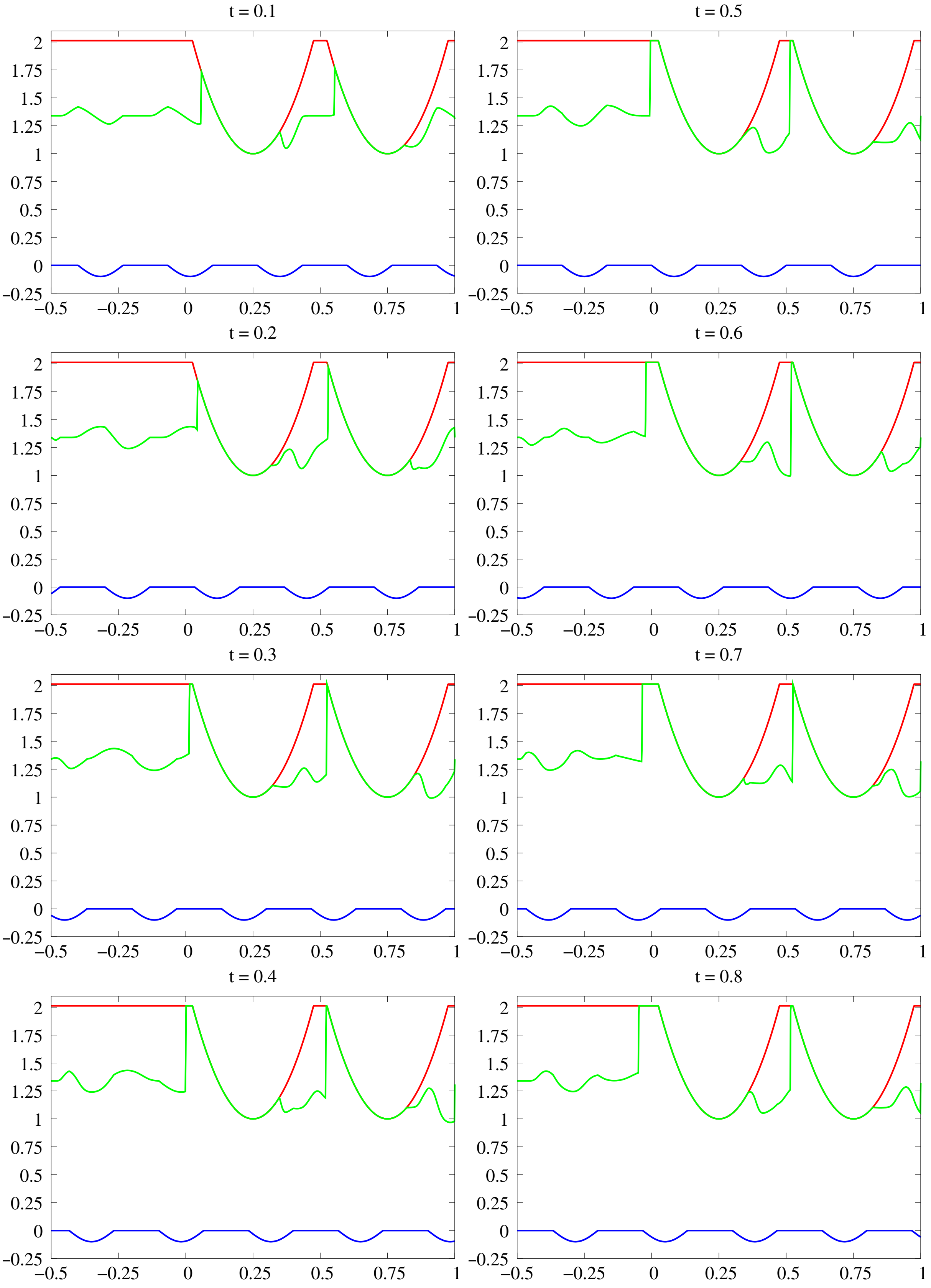

Figure 12: Film profiles at different times for the textured–liner test using the p–θ model.

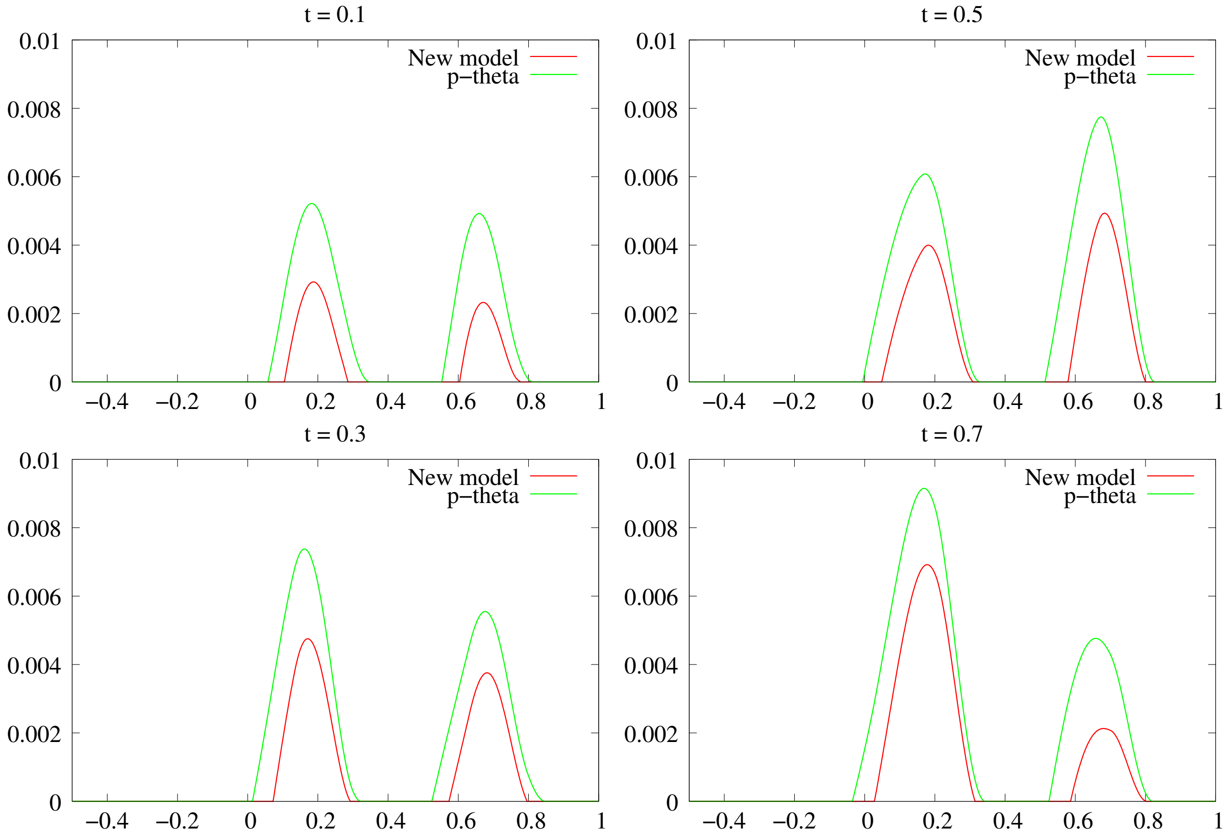

Figure 13: Comparison of non–dimensional pressure profiles at different times using the new model (red) and the p–θ model (green).

differences between the two models. The extension of the present numerical scheme to two dimensions and to the case of a time dependent sliding velocity (of alternating sign) are left for future works.

ACKNOWLEDGMENTS

The authors acknowledge partial support from FAPESP (Brazil), CNPq (Brazil) and Renault (France). This research was carried out in the framework of INCT-MACC, Ministério de Ciência e Tecnologia, Brazil.

REFERENCES

Ausas R., Jai M., and Buscaglia G. A mass–conserving algorithm for dynamical lubrication problems with cavitation. *ASME Journal of Tribology*, 132:031702 (7 pages), 2009.

Ausas R., Ragot P., Leiva J., Jai M., Bayada G., and Buscaglia G. The impact of the cavitation model in the analysis of micro-textured lubricated journal bearings. *ASME Journal of Tribology*, 129:868, 2007.

Buscaglia G., Ciuperca I., and Jai M. A new cavitation model in lubrication. *submitted*, 2011.

Buscaglia G., Jai M., Cadalenc J.P., and Choukrounc F. Mass–conserving numerical simulation of pisto ring/liner contact along a full engine cycle. *Mecánica Computacional*, XXIX:3257–3279, 2010.

Elrod H.G. and Adams M. A computer program for cavitation. Technical report 190. *1st*

LEEDS LYON Symposium on Cavitation and Related Phenomena in Lubrication, I.M.E., 103:354, 1974.

Jakobson B. and Floberg L. The finite journal bearing considering vaporization. *Tran. Chalmers University of Technology*, page 354, 1957.

Olsson K. Cavitation in dynamically loaded bearings. *Tran. Chalmers University of Technology*, 308, 1965.

Priest M. *The wear and lubrication of piston rings*. Ph.D. thesis, University of Leeds, 1996.

Priest M. Factors influencing boundary friction and wear of piston rings. *Tribology series*, 38:409–416, 2000.

Priest M. and Dowson D.and Taylor C.M. Predictive wear modelling of lubricated piston rings in a diesel engine. *Wear*, 231(1):89–101, 1999.